



ELSEVIER

Available online at www.sciencedirect.com

SCIENCE @ DIRECT®

MICROPOROUS AND  
MESOPOROUS MATERIALS

Microporous and Mesoporous Materials xxx (2006) 71–80

www.elsevier.com/locate/micromeso

# Ordered mesoporous $\text{CoO}_x/\text{MCM-41}$ materials exhibiting long-range self-organized nanostructured morphology

A.P. Katsoulidis<sup>a</sup>, D.E. Petrakis<sup>a</sup>, G.S. Armatas<sup>a,b</sup>, P.N. Trikalitis<sup>c</sup>, P.J. Pomonis<sup>a,\*</sup>

<sup>a</sup> Department of Chemistry, University of Ioannina, Ioannina 45110, Greece

<sup>b</sup> Department of Chemistry, Michigan State University, East Lansing, MI 48824, USA

<sup>c</sup> Department of Chemistry, University of Crete, Heraklion 71409, Greece

Received 25 October 2005; received in revised form 20 December 2005; accepted 4 January 2006

## Abstract

A novel class of nanostructured silicious materials of MCM-41 type containing cobalt,  $\text{CoO}_x/\text{MCM-41}$ , and exhibiting remarkable long-range self-organized morphology has been developed. The method of synthesis is a *one step procedure* and includes the use of poly-acrylic acid, complexed with CTAB by a zip-type mechanism, as a backbone of the structure. On the external surface of this meso-structure, hydrolysis of TEOS and  $\text{Co}(\text{NO}_3)_2$  takes place at various pH values. The loading of cobalt ( $9 < \text{Si}/\text{Co} < 37$ ) in the final solid can be controlled by the pH values at which the material is isolated in the range  $5.5 < \text{pH} < 9.5$ . The isolated mesostructures, after drying (80 °C), as well as the resulting mesoporous solids after calcination (600 °C), exhibit remarkable self-organized morphology of the order of  $\mu\text{m}$ . In XRD, both the dried mesostructured as well as the calcined solids, exhibit typical patterns of MCM-41 type, which are blurred as the amount of cobalt increases. The surface area of those nanostructured mesoporous solids  $\text{CoO}_x/\text{MCM-41}$  was determined in the range 910–1250  $\text{m}^2/\text{g}$  by nitrogen porosimetry and their pore volume in the range 0.7–0.9  $\text{cm}^3/\text{g}$ . The pore diameter  $D$  was found to be around 3.1 nm while the pore anisotropy  $b = L/D$ , where  $L$ —the length of the pores, was determined in the range 15–380 depending on the sample. © 2006 Elsevier Inc. All rights reserved.

**Keywords:** MCM-41; Cobalt oxide; Self-assembly; Pore anisotropy; Morphosynthesis

## 1. Introduction

The incorporation of transition metal ions (t.m.i.) into the framework of mesoporous materials, like MCM-41 [1,2], MCM-48 [3,4] and SBA-1 [5,6] has attracted enormous interest due to potential applications of such solids as heterogeneous catalysts [7–12] or electrochemical sensors [13,14]. The most common heteroatoms, which have been incorporated into the silicate framework of silicate mesoporous solids, include Al [15–17], Ga [18,19], Ti [20–22], Mn [23,24] and Co [25–31]. The incorporation of cations like Al and Ti into the  $\text{SiO}_2$  matrix results in a substantial increase of surface acidity [32–34], as happens with

zeolites too [35,36], and such solids can be employed as acid catalysts. On the other hand incorporation of cations like Mn, Ni and Co leads to materials with sites suitable for redox catalytic operations. In relation to cobalt, which is the subject of this work, its incorporation into mesoporous materials has been achieved by direct one pot synthesis [25–27], by post synthesis ion exchange [28–30] as well by gas phase deposition of  $\text{Co}_2(\text{CO})_8$  into the silicate porous network [31]. The content of cobalt loading in the cases of direct synthesis or cation exchange reaches an upper limit of about 10% [25–30] and only in the case of deposition from the gas phase the loading increases to almost 40% for reasons which can be easily understood.

The direct one-pot-synthesis methods are relatively easy procedures, which provide mesostructures or mesoporous solids into which  $\text{CoO}$  or  $\text{Co}_3\text{O}_4$  species are observed depending on the preparation method. In a recent study

\* Corresponding author. Tel.: +30 2651098350; fax: +30 2651098795.  
E-mail address: ppomonis@cc.uoi.gr (P.J. Pomonis).

by Vralstad et al. it was suggested that the amount of cobalt incorporated into the final MCM-41 ( $0.45 < \text{wt.}\% \text{Co} < 4.66$ ) and the MCM-48 ( $0 < \text{wt.}\% \text{Co} < 9.35$ ) solids depends on the pH values which affect the precipitation of cobalt hydroxide  $\text{Co}(\text{OH})_2$  in a mixed gel with oxyhydroxy-silicates [25]. The same authors observed that the addition of increasing amounts of cobalt salt into the MCM-48 synthesis gel causes a change of the mesoporous structure from cubic to hexagonal for reasons related to the charge density matching between the divalent cobalt(II) and the negatively charged silicate species.

In a relevant work by Haskouri et al. on  $\text{CoO}$ -MCM-41 nanocomposites [27] with ratio  $\text{Si}/\text{Co} > 23$  it was shown that the ordered hexagonal structure is degenerated to a wormhole-like structure as the cobalt content increases. Furthermore, independently of the  $\text{Si}/\text{Co}$  ratio, it was observed by UV-vis and NMR techniques that cobalt is organized into the silicate framework in well-dispersed, uniform  $\text{CoO}$  superparamagnetic nanodomains of size approximately 3 nm.

Finally in another publication by Lim et al. [26] highly ordered  $\text{Co}$ -MCM-41 materials were synthesized as catalysts for the production of single wall carbon nanotubes. The local environment of cobalt, as determined by UV-vis spectroscopy, was a mixture of tetrahedral and distorted tetrahedral structures similar to those observed in  $\text{Co}_3\text{O}_4$ . Cobalt appears uniformly distributed at nearly atomic dispersion as probed by XAFS.

In the present paper we communicate a different one-pot-synthesis-method of  $\text{CoO}_x$ -MCM-41 materials, in which, apart from the usual ingredients, i.e. a surfactant CTAB, a silica source TEOS and a source of Cobalt, employed in the above mentioned cases [25–27], we employed poly-acrylic acid as a directing agent of the structure [37–39]. The most remarkable result of this methodology is that it leads to self-organized solid particles, which in the  $\mu\text{m}$  level exhibit long-range decorated patterns of specific morphology, while in the nm level they are typical ordered MCM-type mesoporous solids. We mention that in the literature there are various examples of morphogenetic systems developed usually via a self-organized mechanism [40–53], including cases where poly-acrylic acid was employed as a component of the hybridic system [44d,45d,54]. Nevertheless such systems are not usually porous. As far as we know morphogenesis effects in porous systems have become apparent only in silicate ordered mesoporous solids prepared by the group of Ozin et al. [42]. In the present case the morphogenesis of the ordered mesoporous silicate structure is generated by the addition of a transition metal ion, namely cobalt.

## 2. Experimental section

### 2.1. Preparation of the samples

The preparation of the mesoporous solids took place according to a methodology developed recently [37–39]

which makes use of poly-acrylic acid—Pac in the next—as a stabilizing agent of the micelle structure. The synthesis took place as follows: Pac (0.7 g, 2000 MW, 99% Aldrich) was dissolved in water (100 ml) under stirring. The pH of the solution was adjusted at 1.7 by the use of  $\text{HCl}$  1 M (3 ml). Then CTAB (3.58 g, 99% Merck) was added. The mixture was heated to  $30^\circ\text{C}$  where a clear solution was obtained. Then TEOS (6 ml, 98% Merck) was introduced as a source of silicon and  $\text{Co}(\text{NO}_3)_2 \cdot 6\text{H}_2\text{O}$  (0.884 g, 98% Fluka) as a source of cobalt with atomic ratio  $\text{Si}/\text{Co} = 9$ . Then the pH of that mixture was slowly increased by dropwise addition of  $\text{NaOH}$  0.1 M. The procedure was repeated four times and the final value of pH was set equal to 5.5–6.5–7.5–8.5–9.5, respectively. Each mixture was aged under stirring for 18 h, filtrated and washed with water (30 ml). The samples were dried for 6 h at  $80^\circ\text{C}$ , then heated up to  $600^\circ\text{C}$  with a heating rate  $3^\circ\text{min}^{-1}$  and stayed there for 1 h under atmospheric conditions.

The materials prepared in this way are designated in the next as  $\text{CoO}_x$ -A-B-C-D-E/MCM-41 where each capital letter corresponds to the pH value (5.5–6.5–7.5–8.5–9.5) where the particular sample was isolated.

### 2.2. Characterization

The characterization of the precursors (uncalcined samples) as well as of the calcined solids took place with the following techniques:

*TG-DTA*: The uncalcined materials were checked for their thermal behaviour by detecting simultaneously the TG and the DTA signals in a STA 449 C *Jupiter* system by Netzsch under air flow (30 ml/min) in the temperature range  $300\text{ K} < T < 1273\text{ K}$  and a heating rate of 10 K/min.

*X-ray diffraction*: The dried precursor materials, as well as the calcined solids, were characterized by XRD in a Bruker Advance P8 system using  $\text{CuK}\alpha$  radiation ( $\lambda=1.5418$ ) with step  $0.02^\circ/\text{s}$ .

*Diffuse reflection UV-visible spectroscopy*: The diffuse reflectance spectra of dried and calcined solids were recorded in the range 250–850 nm at room temperature using a UV-vis spectrometer type UV-2401PC by Shimadzu.

*Nitrogen adsorption-desorption porosimetry*: The calcined samples were tested for their surface area and porosity by  $\text{N}_2$  adsorption-desorption porosimetry (77 K) in a Sorptomatic 1990 Fisons porosimeter. Before each measurement the sample was degassed at  $150^\circ\text{C}$  for 6 h.

*SEM-EDS*: The dried precursor materials, as well as the calcined solids, were photographed by scanning electron microscopy (SEM) in a Jeol JSM 5600 system operating at 20 kV. The atomic ratio between  $\text{Si}/\text{Co}$  for each calcined sample was calculated by the average of six measurements of energy dispersive spectra (EDS), which were analysed by the ISIS Oxford Microanalysis system.

**TEM:** Transmission electron micrographs were obtained with a Jeol 100CX instrument equipped with tungsten filament and operating at 100 kV. TEM samples were prepared by casting the powders on a holey carbon grid.

### 3. Results

The main characteristics of calcined samples are listed in Table 1. The content of cobalt increases with the values of pH from Si/Co = 36.7 at pH = 5.5 to Si/Co = 23.6 at pH = 6.5, then to Si/Co = 16.8 at pH = 7.5, Si/Co = 9.9 at pH = 8.5 and finally Si/Co = 9.3 at pH = 9.5. This final composition obtained for the CoO<sub>x</sub>-E/MCM-41 sample is

almost similar to the composition of the original solution Si/Co = 9. This means that at this high pH, silicon and cobalt are quantitatively hydrolyzed and precipitated, forming the inorganic walls of the mesostructure.

The XRD patterns of all samples are presented in Fig. 1. The uncalcined samples (first row) show Bragg reflections indexed in the two-dimension hexagonal system so they are characterized as mesostructured MCM-41 type materials. In the case of calcined samples (second row) the XRD patterns display a decrease of the hexagonal order, especially of those samples were prepared at high pH values (8.5–9.5) in which the content of Co is also high. These samples are characterized as disordered hexagonal mesoporous materials. Moreover the mesoporous materials exhibit a small contraction of the unit cell as indicated by

Table 1  
Atomic ratio Si/Co, specific surface area, pore volume, pore diameter and pore anisotropy of the corresponding samples

Sample	pH	Ratio Si/Co EDS	$S_p$ (m <sup>2</sup> g <sup>-1</sup> ) BET	Pore volume $V_p$ (cm <sup>3</sup> g <sup>-1</sup> )	Pore diameter $D_{p(max)}$ HK (Å)	Hydraulic pore diameter $D_{p(mean)} = 4V_p/S_p$	Pore anisotropy
CoO <sub>x</sub> -A/MCM-41	5.5	36.7	1247	0.77	26	24.7	15
CoO <sub>x</sub> -B/MCM-41	6.5	23.6	1030	0.84	31	32.6	382
CoO <sub>x</sub> -C/MCM-41	7.5	16.8	977	0.85	31	34.8	244
CoO <sub>x</sub> -D/MCM-41	8.5	9.9	911	0.72	31	31.6	63
CoO <sub>x</sub> -E/MCM-41	9.5	9.3	967	0.83	31	34.3	120

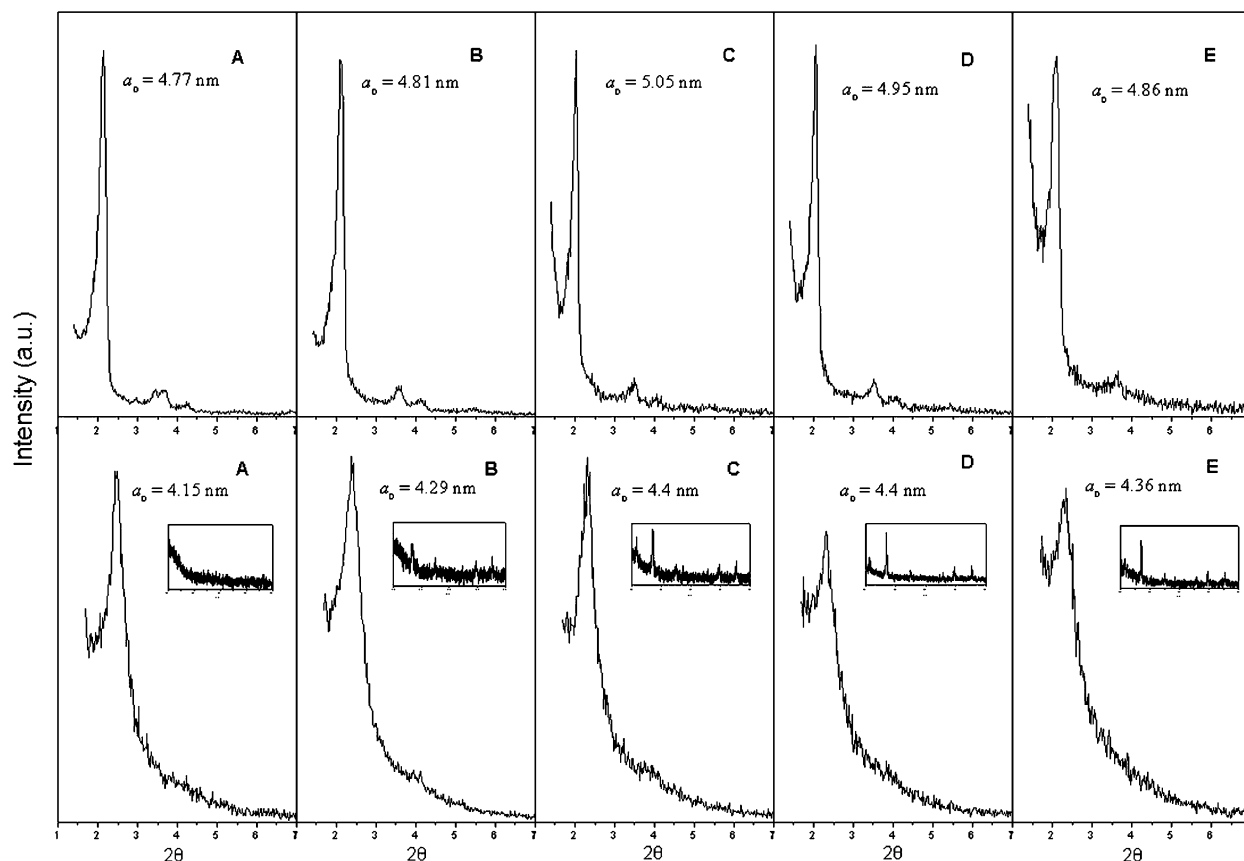


Fig. 1. Low angle XRD patterns of CoO<sub>x</sub>-A–B–C–D–E/MCM-41 uncalcined samples (first row) and calcined samples (second row). In the insets the XRD patterns at high angles with the peaks corresponding to Co<sub>3</sub>O<sub>4</sub>.

the shift of the (100) reflection (see Fig. 1). In the XRD patterns at high angles 30–70° (see insets in the second row in Fig. 1) we can distinguish some reflections corresponding to the crystalline phase  $\text{Co}_3\text{O}_4$ . The low intensity of these peaks in comparison to the background indicates that  $\text{Co}_3\text{O}_4$  particles are small and highly dispersed in the mesoporous structure.

In Fig. 2 the graphs of thermal analysis (TG–DTA) for the uncalcined samples are shown. The weight loss and the exothermic peaks detected from 150 °C to 500 °C are attributed to the nitrates decomposition and the combustion of the organic matter (Pac–CTAB). The combustion is completed at a progressively lower temperature as we proceed from sample  $\text{CoO}_x\text{-A/MCM-41}$  to sample  $\text{CoO}_x\text{-E/MCM-41}$ . This is in agreement to the increasing content of  $\text{CoO}_x$  across the sequence  $\text{A} \rightarrow \text{B} \rightarrow \text{C} \rightarrow \text{D} \rightarrow \text{E}$  of the samples which act as catalysts for both reactions. We also observe a change in the reaction mechanism as D and E samples exhibit one more exothermic shoulder around 210 °C, which should also be due to the increased catalytic action of cobalt in those samples.

In order to investigate the local environment of Co in the mesostructures, as well as in the mesoporous materials, all samples were analysed by diffuse reflectance (DR) UV–vis spectroscopy. The upper part in Fig. 3 illustrates the DR spectra of the dried uncalcined samples that show two bands around 540 and 585 nm and a shoulder around

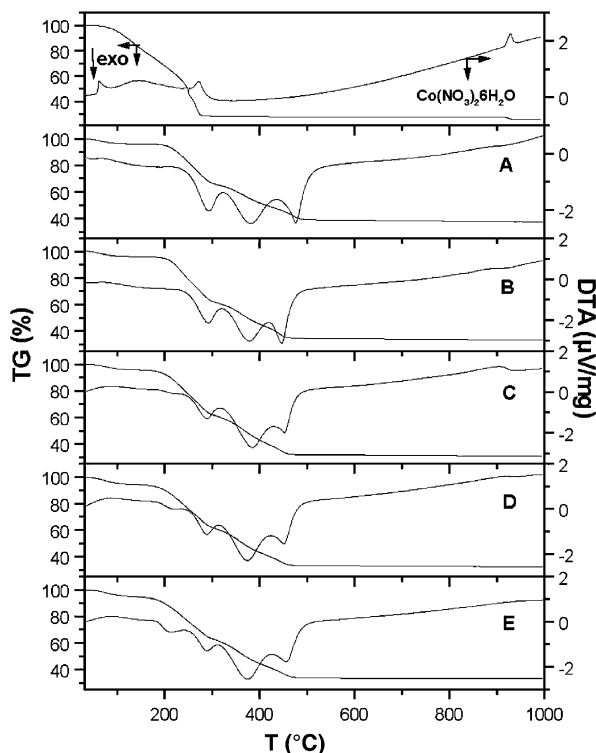


Fig. 2. TG/DTA for the  $\text{CoO}_x\text{-A-B-C-D-E/MCM-41}$  precursors and for  $\text{Co}(\text{NO}_3)_2 \cdot 6\text{H}_2\text{O}$ .

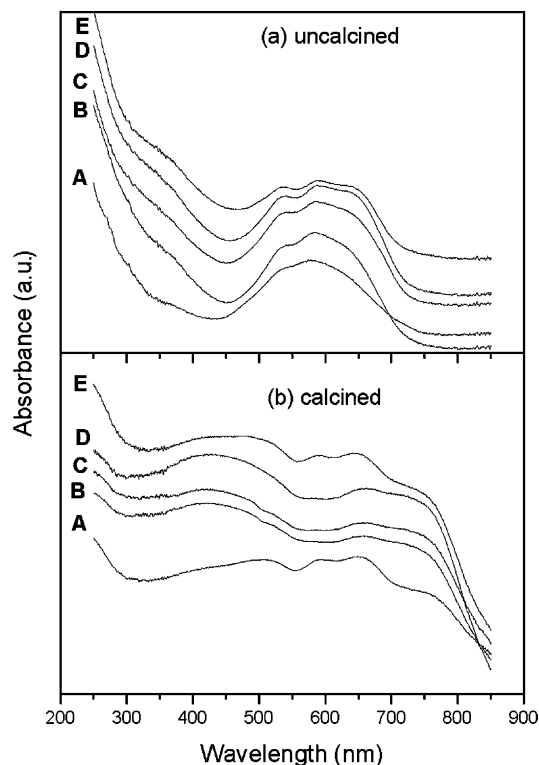


Fig. 3. Diffuse reflectance (DR) spectra of the  $\text{CoO}_x\text{-A-B-C-D-E/MCM-41}$ : (a) uncalcined and (b) calcined materials.

630 nm. This triplet can be assigned to the electronic ligand-field  ${}^4\text{A}_2(\text{F}) \rightarrow {}^4\text{T}_1(\text{P})$  transition for tetrahedrally coordinated  $\text{Co}^{2+}$ . The samples with great content of Co display more intense absorption bands and they have darker blue colour in comparison to the samples with low Co content. During calcination part of  $\text{Co}^{2+}$  had been oxidized to  $\text{Co}^{3+}$  so the DR spectra (Fig. 3) of the samples B, C, D and E show a broad absorption band around 420 nm that is attributed to octahedral coordination of  $\text{Co}^{3+}$  in the mixed valence spinel oxide  $\text{Co}_3\text{O}_4$ . Its absence from the sample A is correlated to the absence of  $\text{Co}_3\text{O}_4$  reflections in the high angle XRD patterns (see inset in Fig. 1). The absorption bands around 585 and 650 nm should be due to the tetrahedrally coordinated  $\text{Co}^{2+}$  in the silica framework [26].

The nitrogen adsorption–desorption isotherms for all the samples A, B, C, D and E are shown in Fig. 4. We do not observe any appreciable hysteresis loop for samples A–D and only sample E exhibits some hysteresis. The condensation of nitrogen in mesopores take place in a broad step for such type of materials and it is correlated to the pore size distribution, which is not narrow. In addition, a knee is observed for all the samples at  $0.30 < P/P_0 < 0.40$ , which is typical of the MCM-41 solids.

The specific surface area  $S_p$  of the solids was estimated by the classical BET methodology by plotting  $(P/P_0)/[V(1 - (P/P_0))]$  vs  $(P/P_0)$  in the range  $0.05 < P/P_0 < 0.25$ . The corresponding values of  $S_p$  determined by this method-

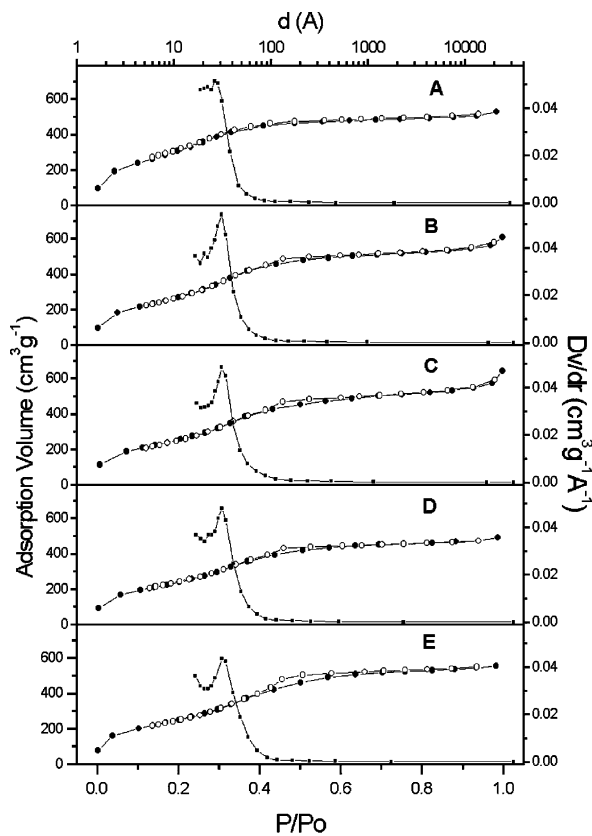


Fig. 4. Nitrogen adsorption–desorption isotherms and the corresponding pore size distribution (HK) for the  $\text{CoO}_x\text{A–B–C–D–E/MCM-41}$  mesoporous solids.

ology are shown in Table 1. In the same table the mean pore diameters of all samples estimated according to Howarth–Kavazoe method (HK) are shown. The sample

A exhibits maxima in the range 26 Å and the rest samples B, C, D and E in 31 Å.

In Fig. 5 some typical SEM microphotographs are shown for all samples. The remarkable feature in those photos is the long-range self-organized morphology for all solids. Their shapes remind bundles, crowns and mushrooms. The appearance of these morphologies at uncalcined materials (Fig. 5c) indicates their formation in the colloidal phase of the synthesis mixture. Their appearance at the calcined materials too (Fig. 5a and b) means that the formed hybridic shapes retain their integrity after the combustion of the organic matter. We draw attention to the fact that the dimensions of these self-organized entities are 1–3  $\mu\text{m}$  in size and the whole collection of particles of the  $\text{CoO}_x\text{A}$ , B/MCM-41 solids exhibit such decorated shapes in SEM, while in the rest C, D and E samples, some particles with random shapes are also apparent.

Finally in Fig. 6 some TEM images of the sample  $\text{CoO}_x\text{A/MCM-41}$  are shown. It was not possible to obtain pictures with higher details because the samples were extremely unstable under electron beam, although images with order porosity were distinguished for a short time. In the first image we observe the hexagonal arrangement of pores with unit cell dimension for about 4 nm, as it was calculated from the XRD patterns. The second image shows that the mesopores of the sample are arranged parallel to the curved edge of the external surface of the particle. This is a very important point meaning that the development of the long-range morphology is takes place by bending of the micelles of the mesophases. In the third image we observe a small particle consisted of aligned parallel pores with mean length 150 nm. This value will be useful when referring to the pore anisotropy in the next section.

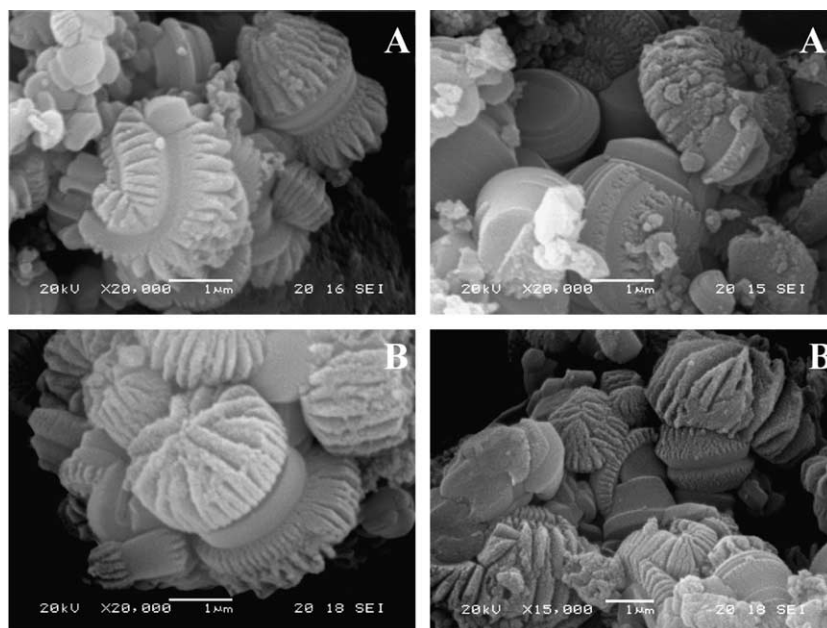


Fig. 5a. SEM photos of calcined samples  $\text{CoO}_x\text{A/MCM-41}$  (first row) and  $\text{CoO}_x\text{B/MCM-41}$  (second row).

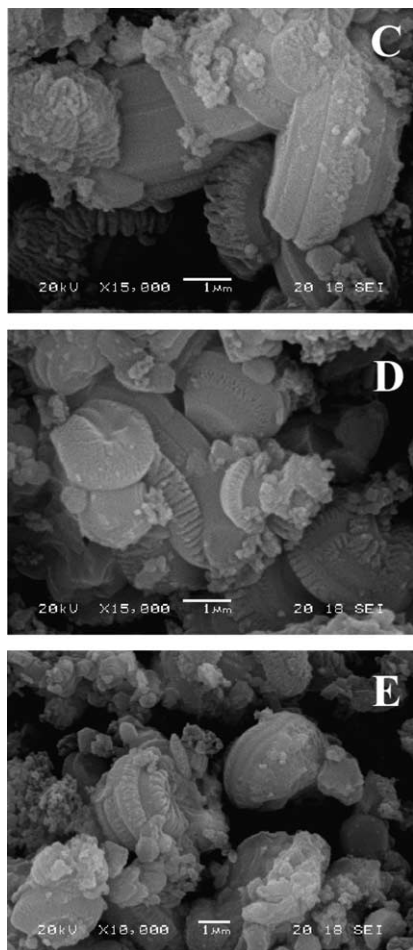


Fig. 5b. SEM photos of calcined samples  $\text{CoO}_x\text{C-D-E/MCM-41}$  in order of appearance from top to bottom.

#### 4. Discussion

As it can be seen from the data in Table 1, the specific surface area  $S_p$  of the solids, estimated by the classical BET methodology is above  $1200 \text{ m}^2/\text{g}$  for sample A, which contains the lower amount of cobalt ( $\text{Si}/\text{Co} = 36.7$ ). Then as the amount of cobalt in the solid increases the values of  $S_p$  decrease to a minimum around  $910 \text{ m}^2/\text{g}$  at ratio  $\text{Si}/\text{Co} = 9.9$  and then increases again to  $967 \text{ m}^2/\text{g}$  as the content of cobalt increases to  $\text{Si}/\text{Co} = 9.3$ . This drop of the specific surface area  $S_p$  is accompanied by the appearance of traces of the phase  $\text{Co}_3\text{O}_4$ , which may block a fraction of mesopores and also by lower ordering of mesopores as observed in the XRD patterns. The Co may be accommodated in two different ways into the structure: either inside to the silica framework in tetrahedral coordination and/or in the form of nanocrystallites of  $\text{Co}_3\text{O}_4$ . The mean size of such crystallites was estimated around 20 nm by the Scherrer equation for the samples C, D and E. However we mention that particles with high content of Co were not detected by SEM-EDS.

We mention that the use of  $a_s$  plot provided nil microporosity for all the samples (see Supplementary information).

The specific pore volume,  $V_p$  ( $\text{cm}^3/\text{g}$ ) is not influenced by the addition of cobalt and remains in the range  $0.73 < V_p < 0.84 \text{ cm}^3/\text{g}$  for all the solids (Table 1). The maximum of the distribution of pore diameter  $D_{p(\text{max})}$  determined according to Howarth-Kavazoe (HK) method is equal to 26 Å for sample A and then remains identical and equal to 31 Å for the rest of the samples. The mean hydraulic pore diameter  $D_{p(\text{mean})} = 4V_p/S_p$  was also determined and found in the range 24.7 Å for the sample A while for the rest it appears larger in the range 32.6–34.8 Å.

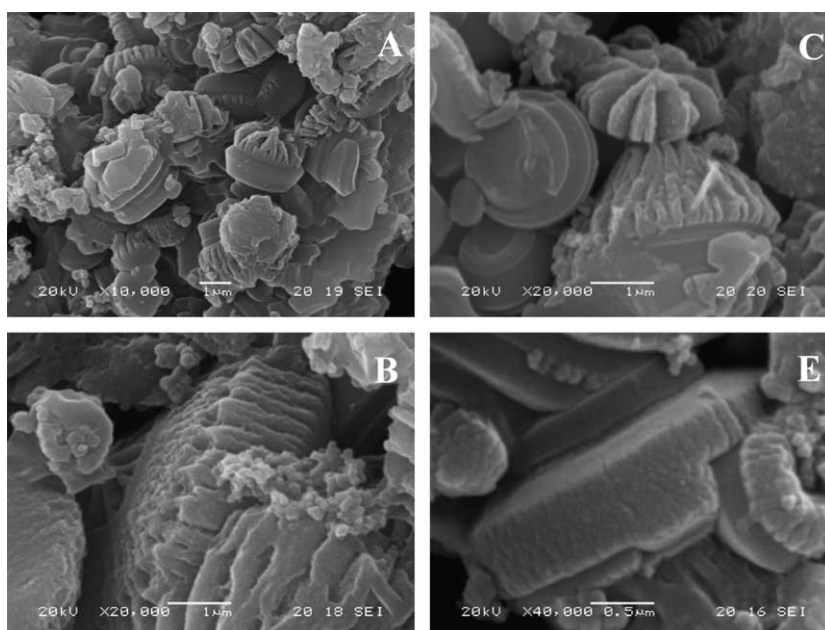


Fig. 5c. SEM photos of uncalcined samples  $\text{CoO}_xA\text{-B-C-E/MCM-41}$ .

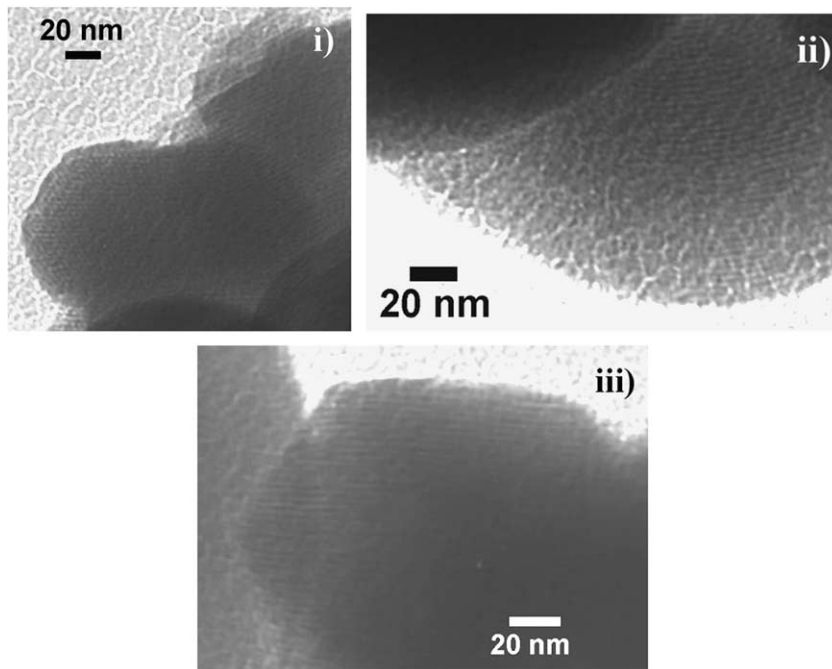


Fig. 6. TEM photos of calcined sample  $\text{CoO}_x\text{A/MCM-41}$ .

#### 4.1. The anisotropy of pores

The estimation of pore anisotropy  $b_i = L_i/D_i$ , where  $L_i$  is the length and  $D_i$  is the diameter of the group  $i$  of pores filled at pressure  $P_i (= P_i/P_0)$ , took place according to a method proposed recently [55]. The purpose was to compare the length of mesopores with the size of the nanostructured particles in order to examine to what extent the pores cross them from one end to the other. The method of estimation, based on the corresponding nitrogen adsorption isotherms, is as follows: The specific surface area  $S_i$  and the specific pore volume  $V_i$  are estimated via a standard algorithm, for example the BJH methodology [56] at each pressure  $P_i (= P_i/P_0)$ . We admit that

$$L_i = D_i b_i = 2r_i b_i = r_i^{a_i} \quad (1)$$

where  $a_i$  is a scaling parameter to be determined. Then the dimensionless ratio  $S_i^3/V_i^2$  is calculated for cylindrical pores according to the relationship

$$\begin{aligned} \frac{S_i^3}{V_i^2} &= \frac{[N_i(2\pi r_i)L_i]^3}{[N_i(\pi r_i^2)L_i]^2} = \frac{[N_i(2\pi r_i)(2r_i b_i)]^3}{[N_i(\pi r_i^2)(2r_i b_i)]^2} = 16\pi b_i N_i \\ &= \frac{[N_i(2\pi r_i)(r_i)^{a_i}]^3}{[N_i(\pi r_i^2)(r_i)^{a_i}]^2} = 16\pi N_i \left( \frac{r_i^{a_i-1}}{2} \right) \end{aligned} \quad (2)$$

where  $N_i$ —the number of pores filled with  $\text{N}_2$  at each pressure  $P_i (= P_i/P_0)$  having radius  $r_i$  and diameter  $D_i$ . The term

$$\lambda_i = (S_i^3/16\pi V_i^2) = N_i b_i \quad (3)$$

corresponds to the *total anisotropy*  $\lambda_i$  of the group  $N_i$  of the pores with anisotropy  $b_i$  each of them. The above Eq. (3), after taking logarithms, obtains the form

$$\log(\lambda_i) = \log\left(\frac{N_i}{2}\right) + (a_i - 1) \log r_i \quad (4)$$

Then the values of the  $a_i$  parameter can be easily calculated from the plots  $\log \lambda_i$  vs  $\log r_i$ . This is shown in Fig. 7 where plots of  $\log \lambda_i$  as a function of  $\log r_i$  as well as a function of  $(P_i/P_0)$  have been drawn in order to illustrate better the case.

From Fig. 7 we observe that the total pore anisotropy  $\lambda_i = N_i b_i$  is very high at low  $(P/P_0)$ . This is because a lot of micropores and ultra-micropores are filled immediately as the partial pressure  $(P_i/P_0)$  increases slightly above zero. Consequently the value of total anisotropy  $\lambda_i$  drops rapidly as  $(P_i/P_0)$  increases because more and more micropores are filled up and eliminated from the counting process. Suddenly at  $(P/P_0) = 0.3$ – $0.4$  where the mesopores are filled (see the  $\text{N}_2$  adsorption isotherms in Fig. 4), the total anisotropy  $\lambda_i$  increases suddenly. This kink is shown better in the plots  $\log \lambda_i$  vs  $\log r_i$  (right hand part in Fig. 7). This is because a lot of mesopores, having large anisotropy  $b_i$ , are suddenly filled up. We mentioned that such a kink is *absent* in non-ordered mesoporous materials and it is observed only in MCM-41 solids [55]. Thereafter the values of total anisotropy  $\lambda_i$  decrease continuously as less and less pores with smaller anisotropy are filled up.

The values of anisotropy  $b_i$  for each group  $i$  of pores are then given by the simple equation

$$b_i = 0.5r_i^{(a_i-1)} \quad (5)$$

The estimated values of  $b_i$  are plotted in Fig. 8 as a function of  $r_i$ , while the maximum values of  $b_i$  found for each porous solid  $\text{CoO}_x\text{-A, B, C, D, E /MCM-41}$  are mentioned in Table 1.

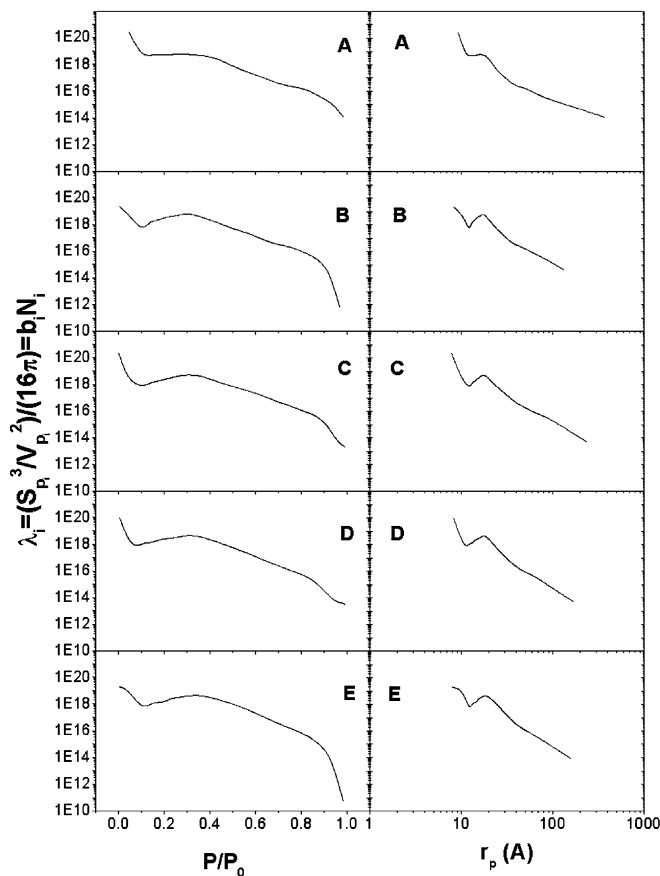


Fig. 7. The total pore anisotropy  $\lambda_i = b_i N_i$  of group  $i$  of  $N_i$  pores, each group having anisotropy  $b_i$ , as a function of pressure  $P_i = P/P_0$  (left) or as a function of the corresponding radius  $r_i$  (right) for the samples A, B, C, D and E.

The values of pore anisotropy  $b_i$  were found in the range  $15 < b_i < 382$ . For pore diameter around  $D_i \sim 30 \text{ \AA}$ , their length is in the range  $450\text{--}11,460 \text{ \AA}$ . We remind that the pores length observed in TEM images are between  $1000$  and  $2000 \text{ \AA}$ . We are not aware of any TEM microphotographs in the literature, which provide enough evidence about the *total length* of pores in similar MCM-41 ordered mesoporous solids. The only data known to us is by Zheng et al. [57] who prepared and studied  $\text{TiO}_x\text{Ny}$  oxynitrided mesoporous silica MCM-14 whose pore length in TEM appears in the range of  $100\text{--}200 \text{ nm}$ , in good agreement with the findings in the present work. Nevertheless if the maximum value of the pore length for sample B is around  $1 \mu\text{m}$ , this is almost equal to the diameter of the particles of that sample shown in the SEM photos in Fig. 5a. In other words those particles should be perforated systems with the pores crossing them from one to the opposite end. This point needs certainly further scrutinization.

#### 4.2. The development of the decorated structures

The ornate and decorated structures of the studied materials are apparent in the whole mass of particles

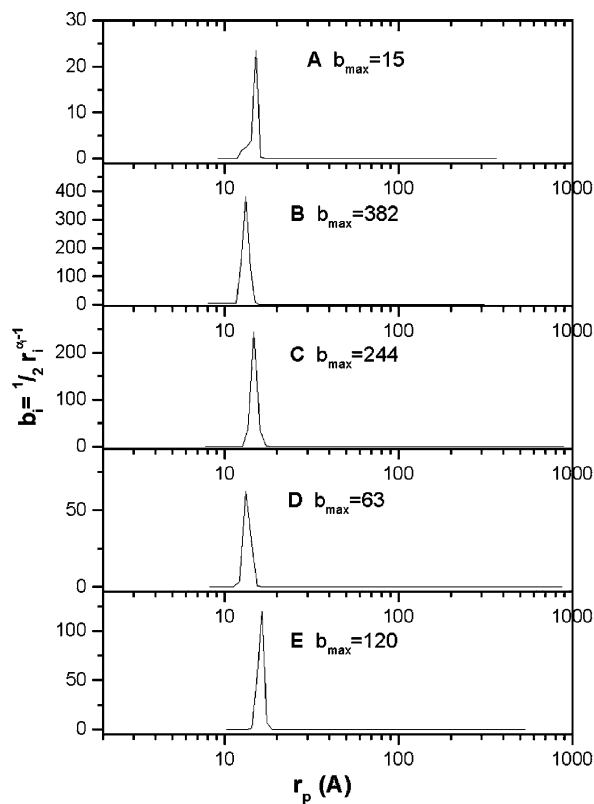


Fig. 8. Variation of pore anisotropy  $b_i$  as a function of its radius  $r_i$  for the  $\text{CoO}_x\text{A-B-C-D-E/MCM-41}$  mesoporous solids.

but they are more clear and profound in samples A and B with low content of cobalt. As the content of cobalt increases in samples  $C \rightarrow D \rightarrow E$ , the decorations appear more and more blurred. The reason should be the content of Co which, in small amounts in A and B samples, organizes the structure while in larger amounts in C, D and E samples covers the details, probably because of hydrolysis and precipitation of  $\text{CoO}_x(\text{OH})_y$  species on and into small cavities of the already self-organized structure. Another reason for the deterioration of the structure might well be the fast condensation of silica at higher pH values.

We have checked this phenomenon of self-organization of the system Pac-CTAB-TEOS using other d-transition metals but the result was disappointing. It seems that it is promoted favourably and almost exclusively by cobalt: The nickel, used in exactly similar experiments not discussed here, has a quite medium effect while manganese showed a very poor performance. Also the addition of a hetero-cation, like La or Ce destroys the order completely. So cobalt should have a special property, or properties, which promotes the development of structures shown in Fig. 5.

The size of the decorated particles in Fig. 5 is as large as  $1\text{--}3 \mu\text{m}$ . From the SEM photographs in this figure we observe that the decoration bears two distinct parts: A *circular disk* in the middle and a *crown* on top of it (see for

example the photo of the uncalcined sample A in Fig. 5c and also the left hand photos for the calcined samples A and B in Fig. 5a). In some cases the crown has been symmetrically developed on both sides of the disk, while in some other cases it has been developed on one side (see for example the right hand photos for samples A and B in Fig. 5a) or it has been cut along the axis vertical to the disk (sample A—left photo). Often the disks appear isolated without any crowns developed on them (calcined samples A and B in the right photos in Fig. 5a and uncalcined samples C and E in Fig. 5c) or the crown has developed itself without the disk (see the big particles of the uncalcined samples B in Fig. 5c). Also it is important that the isolated disks show distinct steps in their circular edge (see uncalcined sample E in Fig. 5c and the calcined samples A-right photo in Fig. 5a and C in Fig. 5b): The crown seems to be developed on those circular steps around the disk. Finally the fully developed crowns show elements of self-similarity: As they start from the disk, they are made up of thin branches, which are coupled to some kind of arches, forming thicker ones which are finally bended and form the top of the crown. The circumference of the crowns, especially of the large ones, is often developed further and outside of the circumference.

How these amazing structures were developed and self-organized? A detail answer to this question is unattainable for the moment. Nevertheless in the literature there are somehow similar examples of morphogenesis leading to similar shapes. Perhaps the best paradigm, in connection to the present case, is the classical studies of the hierarchically ordered spherical aggregates of fluoroapatite, studied in remarkable details by Kniep et al. [44a,44b]. It was shown that in a gelatin medium such particles are developed from an hexagonal prismatic seed on which successive generations of crystallites are tilted mounted with their main axis increasingly inclined with respect to the orientation of the seed. As a result a successive skewing is imposed on the development of the macrocrystal, with respect to the alignment of the seed, which leads to a nearly isotropic distribution of crystallites towards two semi-spheres and eventually to a nearly perfect sphere.

In a similar fashion the dumbbell morphologies of  $\text{CaCO}_3$  particles developed in the presence of PEG–PMAA by Colfen and coworkers [45b] as well as of  $\text{BaCO}_3$  particles developed in the presence of PSS–PAH by Yu et al. [45c] were attributed to a captured intermediate stage evolving from aggregates of small and often rodlike nanocrystallites which, via dumbbells, lead to spheres. The materials of the present study seem to represent intermediate captured stages of such a scenario for which many questions await scrutinization.

In conclusion, we prepared MCM-41 structures containing small amounts of cobalt which generates long-range and self-organized morphogenetic features on them. Those materials possess high surface area and pore anisotropy calculations indicated that most probably the pores run across the whole particles.

## Acknowledgments

We acknowledge financial support from the project PYTHAGORAS finance from EU and the Ministry of Education (project EPEAEK) and the project PENED 2003 from the General Secretariat of Research and Technology (GSRT). We also acknowledge technical support from the Network of Laboratory Units and Centers of the University of Ioannina for the TG–DTA, SEM–EDS and XRD measurements and the TEM facility of the University of Crete. We are also indebted to Dr N. Kourkoumelis and L. Karwacki for their help.

## Appendix A. Supplementary data

Supplementary data associated with this article can be found, in the online version, at [doi:10.1016/j.micromeso.2006.01.001](https://doi.org/10.1016/j.micromeso.2006.01.001).

## References

- [1] J.S. Beck, J.C. Vartuli, W.J. Roth, M.E. Leonowicz, C.T. Kresge, K.D. Schmitt, C.T.-W. Chu, D.H. Olson, E.W. Sheppard, S.B. McCullen, J.B. Higgins, J.L. Schlenker, *J. Am. Chem. Soc.* 114 (1992) 10834.
- [2] Q. Huo, D.I. Margolese, U. Ciesla, P. Feng, T.E. Gier, P. Sieger, R. Leon, P.M. Petroff, F. Schuth, G.D. Stucky, *Nature* 368 (1994) 317.
- [3] Q. Huo, D.I. Margolese, U. Ciesla, D.K. Demuth, P. Feng, T.E. Gier, P. Sieger, A. Firouzi, B.F. Chmelka, F. Schüth, G.D. Stucky, *Chem. Mater.* 6 (1994) 1176.
- [4] A. Monnier, F. Schüth, Q. Huo, D. Kumar, D. Margolese, R.S. Maxwell, G.D. Stucky, M. Krishnamurty, P. Petroff, A. Firouzi, M. Janicke, B.F. Chmelka, *Science* 261 (1993) 1299.
- [5] D. Zhao, J. Feng, Q. Huo, N. Melosh, G.H. Fredrickson, B.F. Chmelka, G.D. Stucky, *Science* 279 (1998) 548.
- [6] D. Zhao, Q. Huo, J. Feng, B.F. Chmelka, G.D. Stucky, *J. Am. Chem. Soc.* 120 (1998) 6024.
- [7] P.T. Tanev, T.J. Pinnavaia, *Science* 271 (1996) 1267.
- [8] W. Zhang, T.R. Pauly, T.J. Pinnavaia, *Chem. Mater.* 9 (1997) 2491.
- [9] A. Corma, *Chem. Rev.* 97 (1997) 2373.
- [10] A. Tuel, *Micropor. Mesopor. Mater.* 27 (1999) 151.
- [11] C. Song, K.M. Reddy, *Appl. Catal. A* 176 (1999) 1.
- [12] A. Jentys, N.H. Pham, H. Vinek, M. Englisch, J.A. Lercher, *Catal. Today* 39 (1998) 311.
- [13] (a) I. Gill, *Chem. Mater.* 13 (2001) 3404;  
(b) S. Dong, X. Chen, *Rev. Mol. Biotech.* 82 (2002) 303;  
(c) W. Jin, J.D. Brennan, *Anal. Chim. Acta* 461 (2002) 1.
- [14] B. Prieto-Simon, G.S. Armatas, P.J. Pomonis, C.G. Nanos, M.I. Prodromidis, *Chem. Mater.* 16 (2004) 1026.
- [15] M.T. Janicke, C.C. Landry, S.C. Christiansen, S. Birtalan, G.D. Stucky, B.F. Chmelka, *Chem. Mater.* 11 (1999) 1342.
- [16] A.A. Romero, M.D. Alba, J. Klinowski, *J. Phys. Chem. B* 102 (1998) 123.
- [17] S. Sklari, H. Rahiala, V. Stathopoulos, J.B. Rosenholm, P.J. Pomonis, *Micropor. Mesopor. Mater.* 49 (2001) 1.
- [18] C.F. Cheng, H. He, W. Zhou, J. Klinowski, J.A.S. Goncalves, L.F. Gladden, *J. Phys. Chem.* 100 (1996) 390.
- [19] M. Chatterjee, T. Iwasaki, Y. Onodera, T. Nagase, H. Hayashi, T. Ebina, *Chem. Mater.* 12 (2000) 1654.
- [20] P.T. Tanev, M. Chibwe, T.J. Pinnavaia, *Nature* 368 (1994) 321.
- [21] M.D. Alba, Z. Luan, J. Klinowski, *J. Phys. Chem.* 100 (1996) 2178.
- [22] J.B. Rosenholm, H. Rahiala, V. Stathopoulos, P.J. Pomonis, I. Beurrois, K. Backfolk, *Colloids Surf. A* 250 (2004) 289.
- [23] J. Zhang, D. Goldfarb, *J. Am. Chem. Soc.* 122 (2000) 7034.

- [24] J. Xu, Z. Luan, M. Hartmann, L. Kevan, *Chem. Mater.* 11 (1999) 2928.
- [25] T. Vrålstad, G. Øye, M. Rønning, W.R. Glomm, M. Stöcker, J. Sjöblom, *Micropor. Mesopor. Mater.* 80 (2005) 291.
- [26] S. Lim, D. Ciuparu, C. Pak, F. Dobek, Y. Chen, D. Harding, L. Pfefferle, G. Haller, *J. Phys. Chem. B* 107 (2003) 11048.
- [27] J. El Haskouri, S. Cabrera, C.J. Gomez-Garcia, C. Guillem, J. Latorre, A. Beltran, D. Beltran, M.D. Marcos, P. Amoros, *Chem. Mater.* 16 (2004) 2805.
- [28] A.D. Badiei, L. Bonnevot, *Inorg. Chem.* 37 (1998) 4142.
- [29] A. Tuel, in: L. Bonnevot, F. Beland, C. Danumah, S. Giasson, S. Kaliaguine (Eds.), *Proceedings of the 1st International Symposium on Mesoporous Molecular Sieves*, *Stud. Surf. Sci. Catal.* vol. 117, Elsevier, Amsterdam, 1998.
- [30] A. Vinu, J. Dedecek, V. Murugesan, M. Hartmann, *Chem. Mater.* 14 (2002) 2433.
- [31] S. Suvanto, J. Hukkamaki, T.T. Pakkanen, T.A. Pakkanen, *Langmuir* 16 (2000) 4109.
- [32] J.M. Campelo, D. Luna, R. Luque, J.M. Marinas, A.A. Romero, J.J. Calvino, M.P. Rodríguez-Luque, *J. Catal.* 230 (2005) 327.
- [33] D. Zhao, C. Nie, Y. Zhou, S. Xia, L. Huang, Q. Li, *Catal. Today* 68 (2001) 11.
- [34] M.L. Occelli, S. Biz, A. Auroux, *Appl. Catal. A* 183 (1999) 231.
- [35] R.M. Barrer, *Hydrothermal Chemistry of Zeolites*, Academic Press, New York, 1982.
- [36] V.N. Romannikov, V.M. Mastikhin, S. Hocevar, B. Drzaj, *Zeolites* 3 (1983) 311.
- [37] C.C. Pantazis, P.N. Trikalitis, P.J. Pomonis, M.J. Hudson, *Micropor. Mesopor. Mater.* 66 (2003) 37.
- [38] C.C. Pantazis, P.J. Pomonis, *Chem. Mater.* 15 (2003) 2299.
- [39] C.C. Pantazis, P.N. Trikalitis, P.J. Pomonis, *J. Phys. Chem. B* 109 (2005) 12574.
- [40] S. Mann, G.A. Ozin, *Nature* 382 (1996) 313.
- [41] Q. Sun, E.G. Vrieling, R.A. van Santen, N.A.J.M. Sommerdijk, *Curr. Opin. Solid State Mater. Sci.* 8 (2004) 111.
- [42] (a) G.A. Ozin, *Can. J. Chem.* 77 (1999) 2001;  
(b) G.A. Ozin, *Acc. Chem. Res.* 30 (1997) 17;  
(c) H. Yang, G. Ozin, C. Kresge, *Adv. Mater.* 10 (1998) 883;  
(d) I. Sokolof, H. Yang, G. Ozin, C. Kresge, *Adv. Mater.* 11 (1999) 636.
- [43] M. Antonietti, G.A. Ozin, *Chem. Eur. J.* 10 (2004) 28.
- [44] (a) For phosphates see R. Kniep, S. Busch, *Angew. Chem. Int. Ed.* 35 (1996) 2623;  
(b) S. Busch, R. Kniep, *Adv. Funct. Mater.* 13 (2003) 189;  
(c) M. Antonietti, M. Breulmann, C.G. Goltner, H. Colfen, K.K.W. Wong, D. Walsh, S. Mann, *Chem. Eur. J.* 4 (1998) 2493;  
(d) A. Bigi, E. Boanini, D. Walsh, S. Mann, *Angew. Chem. Int. Ed.* 41 (2002) 2163.
- [45] (a) For carbonates see H. Colfen, *Curr. Opin. Colloid Interf. Sci.* 8 (2003) 23;  
(b) H. Colfen, L. Qi, *Chem. Eur. J.* 7 (2001) 106;  
(c) S.H. Yu, H. Colfen, A.W. Xu, W. Dong, *Cryst. Growth Des.* 4 (2004) 33;  
(d) A. Sugawara, T. Ishii, T. Kato, *Angew. Chem. Int. Ed.* 42 (2003) 5299.
- [46] (a) For sulfates see L. Qi, H. Colfen, M. Antonietti, M. Li, J.D. Hopwood, A.J. Ashley, S. Mann, *Chem. Eur. J.* 7 (2001) 3526;  
(b) L. Qi, H. Colfen, M. Antonietti, *Angew. Chem. Int. Ed.* 39 (2000) 604;  
(c) M. Li, S. Mann, *Langmuir* 16 (2000) 7088.
- [47] For chromates see H. Shi, L. Qi, J. Ma, H. Cheng, B. Zhu, *Adv. Mater.* 15 (2003) 1647.
- [48] (a) For metal oxides see R.A. Caruso, *Angew. Chem. Int. Ed.* 43 (2004) 2746;  
(b) D. Yang, L. Qi, J. Ma, *Adv. Mater.* 14 (2002) 1543;  
(c) J. Huang, T. Kunitake, *J. Am. Chem. Soc.* 125 (2003) 111834.
- [49] (a) For metal hydroxides see A.K. Boal, T.J. Headley, R.G. Tissot, B.C. Bunker, *Adv. Funct. Mater.* 14 (2004) 19;  
(b) I. Ichimose, K. Kurashima, T. Kunitake, *J. Am. Chem. Soc.* 126 (2004) 7162.
- [50] (a) For tungstates see S.H. Yu, B. Liu, M.S. Mo, J.H. Huang, X.M. Liu, Y.T. Qian, *Adv. Funct. Mater.* 13 (2003) 639;  
(b) H. Shi, L. Qi, J. Ma, H. Cheng, *J. Am. Chem. Soc.* 125 (2003) 3450.
- [51] (a) For sulfides see Q. Lu, F. Gao, S. Komarneni, *J. Am. Chem. Soc.* 126 (2004) 54;  
(b) Y. Ma, L. Qi, J. Ma, H. Cheng, *Langmuir* 19 (2003) 4040.
- [52] For carbon see S. Polarz, B. Smarsly, J.H. Schattka, *Chem. Mater.* 14 (2002) 2940.
- [53] (a) For trimodal silica see K. Suzuki, K. Ikari, H. Imai, *J. Mater. Chem.* 13 (2003) 1812;  
(b) D. Kuang, T. Brezenski, B. Smarsly, *J. Am. Chem. Soc.* 126 (2004) 10534.
- [54] (a) A. Kotachi, T. Miura, H. Imai, *Chem. Mater.* 16 (2004) 3191;  
(b) Y. Oaki, H. Imai, *Langmuir* 21 (2005) 863;  
(c) Y. Oaki, H. Imai, *Adv. Funct. Mater.* 15 (2005) 1407.
- [55] P.J. Pomonis, G.S. Armatas, *Langmuir* 20 (2004) 6719.
- [56] E.P. Barrett, L.G. Joyner, P.P. Halenda, *J. Am. Chem. Soc.* 73 (1951) 373.
- [57] S. Zheng, Z. Li, L. Gao, *Mater. Chem. Phys.* 85 (2004) 195.